

Effect of substrate crystal type on properties of oblique angle sputtered barium strontium titanate ($\text{Ba}_{0.5}\text{Sr}_{0.5}\text{TiO}_3$) thin films

MOHAMAD JAVAD ESHRAGHI*, MAHDI BORDBARI, NIMA NADERI,
ALI SEDAGHAT AHANGARI HOSSEINZADEH
Materials and Energy Research Center, Karaj, Iran

The substrate type effect on properties of oblique angle sputter deposited Barium strontium titanate films have been investigated. The thickness of the layers decreased with increasing deposition angle. The dependence of optical properties of deposited films on substrate types was studied using reflectometry. The electrical properties of films also were characterized by I-V measurement in an appropriate range. It has been found that the effective refractive index of deposited films was changed due to the variation in surface morphology which caused a redshift in the peak position of the reflectance spectrum. The substrate material and the deposition angle affected the grain size of the synthesized layers, which results in variation in the porosity of deposited layers. Improvements in electrical conductivity were observed in the coated samples on polycrystalline and amorphous substrates. Deposition on glass substrate results in increased grain size and decreased electrical resistance with respect to alumina substrate. Increasing the deposition angle also increased the grain size.

(Received February 21, 2022; accepted October 6, 2023)

Keywords: Barium strontium titanate, Substrate effect, Oblique angle deposition, Reflectometry, Grain size, Surface porosity

1. Introduction

The crystal structure has a great effect on the physical and chemical properties of a compound[1]. Recently, the crystal structure control of materials has been the subject of many studies in the synthesis process to create the desired properties[2], [3]. The predictability of the structure and properties of the synthesized thin layer can help in choosing suitable substrates and layer deposition conditions for the intended application[4]–[6] which could also reduce production process costs. The morphological control of the layer's structure allows control of the prepared layer's properties[7], [8]. Optical properties[2] such as refractive index[9], transmission, reflection, and light absorption can be controlled. In addition, the structure of the layer plays an important role in the creation of chemical properties such as anti-corrosion[10], [11], etching rate[12], gas[13] and liquid[14] penetration, and catalytic processes[15].

The structure of deposited layers can alter the physical and chemical properties of layers. The structural changes can be applied before, during and after layer formation. Some of the parameters affecting the structure of deposited layers are precursor materials[16], substrates phase[16] and seed implantation [17]. Deposition conditions such as substrate-target geometrical configuration[18], substrate temperature[19], deposition method[20], and other deposition parameters[21] are some of the factors which can help to achieve special structure during deposition process. Substrate features such as atomic and crystalline structures can influence the final properties of the deposited layer[22], [23]. For example, a crystalline

substrate can affect the arrangement of the atoms in the deposited layer and cause changes in its bandgap[24], while the amorphous substrate will have less effect on the organization of the deposited layer atoms. On the other hand etching[25] and annealing[26] can be effective for structure modifications after layer forming.

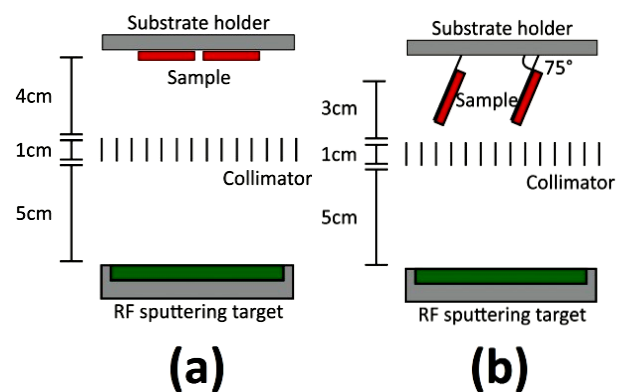


Fig. 1. The schematic of layer deposition configuration (a) regular deposition under 0° and (b) tilted deposition under 75° (color online)

Barium strontium titanate, $\text{Ba}_x\text{Sr}_{1-x}\text{TiO}_3$ (BST) due to its ferroelectric properties such as wide bandgap, high refractive index, low light absorption[27], large dielectric constant[28], [29] and high electrical resistivity[30] has attracted the attention of many researchers. BST in electronic industries is used in many applications such as supercapacitor[31] and non-volatile memories[32], [33].

Oblique angle deposition is a technique for the fabrication of nanostructured arrays[18], [34]. This method is a modification of typical physical vapor deposition (PVD) such as electron beam evaporation and sputtering with a tilted substrate[18]. Figure 1 shows the schematic of oblique angle deposition kinetic for nanostructure formation using a PVD technique with an oblique angle. Here, when the deposition flux reaches the substrate with an oblique angle, there will be a change in the mechanism of deposition which has a significant influence on the development of the microstructure and compactness of deposited layers[35]–[37]. Here, the initial particles grow on the nucleation sites and lead to the formation of nanocolumns tilted towards the vapor flux direction[18], [35], [38]. This simple and efficient fabrication technique has been used to grow well-aligned nanostructures[37], [39].

This work focuses on the influence of substrate material and crystalline structure on the deposition behavior of deposited layers and its effect on the physical properties of the deposited BST layers such as crystal plane preference, roughness, crystallite size, strain, surface porosity, light reflection, and especially electrical resistance.

2. Experimental procedure

Three substrate types, i.e. single crystalline (silicon wafer 111 p-type), polycrystalline (alumina wafer), and amorphous (soda-lime glass) were used with a dimension of 10mm×10mm×0.5mm. Before deposition substrates were ultrasonically rinsed in deionized water and ethanol solution for 6 minutes, then rinsed with deionized water for 1 minute and dried at 70° C under atmosphere.

Samples were installed on the holder 0° and 75° aligned with respect to the perpendicular line between the holder and the sputtering target. An 8mm×8mm collimator grid with 8mm thickness installed parallel to sputtering target between target and holder to make particle flow directional and consequently facilitate the formation of random primary seeds on substrates and nanostructure on samples surface. Lab-made Ba_{0.5}Sr_{0.5}TiO₃ sputtering target used as a deposition source[40]. Sputtering was performed in pure argon atmosphere under 5.6×10⁻³ mbar pressure and RF power of 122 W for 120 min without heating the substrates during the deposition[41,42]. The configuration of layer deposition is schematically shown in Fig. 1. After deposition, samples were annealed at 350°C for 1h under the atmosphere.

To study the substrate type effect on the properties of deposited layers several analysis methods were implemented. Scanning electron microscopy (SEM, FEI Quanta 200) was used to investigate the surface morphology and thickness of deposited layers. Grazing incidence x-ray diffraction (GIXRD, Philips PW1730 with copper tube) was used for determining crystallite size, strain, and crystalline phase. Profile of height distribution on the surface was obtained using atomic force microscopy (AFM, Park Scientific Instruments Autoprobe

CP) which was used to calculate surface roughness. The I-V characteristics were measured by applying a voltage to samples by source meter (KEITHLEY 2400) which was used to calculate the electrical resistivity of layers using ohm's law[43]. The reflectance intensity was measured by a spectrophotometer (PHYSTEC IRAN) with visible light source.

The thickness and surface porosity of layers were estimated using SEM images and *ImageJ* software. Crystallite size, strain, and phases of crystal structure were obtained by the Williamson-Hall equation and compared with JCPDS file no. 00-039-1395 (Ba_{0.5}Sr_{0.5}TiO₃) from the GXRDP pattern. XRD pattern was smoothed in *HighScore Plus* software using a fast Fourier transform method. Crystallite size and strain in layer structure were obtained using the Williamson-Hall equation expressed below[44]:

$$FWHM \times \cos \theta = \frac{K\lambda}{\text{crystallite size}} + 4 \times \sin \theta \times \text{strain}(\%) \quad (1)$$

where K is a constant equal to 0.94, $FWHM$ is full width at half maximum of XRD peak, θ is the peak position, and λ is the wavelength of radiation (1.54056 Å for copper tube K_{α1} radiation).

The surface roughness of layers was calculated by *WSXM5* software using surface height profiles that were measured with AFM analysis and calculated by the following equation[45]:

$$R_q = \left(\sum_{i=1}^N \frac{Z_i^2}{N} \right)^{\frac{1}{2}} \quad (2)$$

where R_q is surface roughness, Z is the height profile of every scanned point, and N is the number of scanned points. The region of AFM probe scanning was a 2μm×2μm surface. The porosity percentage was calculated using the following equation[46]:

$$V_{\text{solid}} = \int_{x_{\min}}^{x_{\max}} \int_{y_{\min}}^{y_{\max}} f(x, y) dx dy \quad (3)$$

$$V_{\text{total}} = f_{\max}(x_{\max} - x_{\min})(y_{\max} - y_{\min}) \quad (4)$$

$$\phi = 1 - \frac{V_{\text{solid}}}{V_{\text{total}}} \quad (5)$$

where V_{total} is the total volume of the surface, V_{solid} is the filled spaces volume in the surface, f_{\max} is the maximum depth difference, $f(x, y)$ is the sample surface height function and ϕ is the surface porosity. The deepest pit and highest peak of surface ruggedness (f_{\max}) differences were considered as the thickness of the surface layer for surface porosity calculation (Fig. 2).

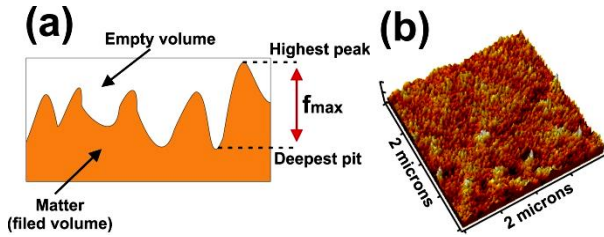


Fig. 2. (a) Cross-sectional schematic of surface roughness, (b) 3D-image of the area scanned by the AFM probe belonging to the sample deposited on glass under 75° (color online)

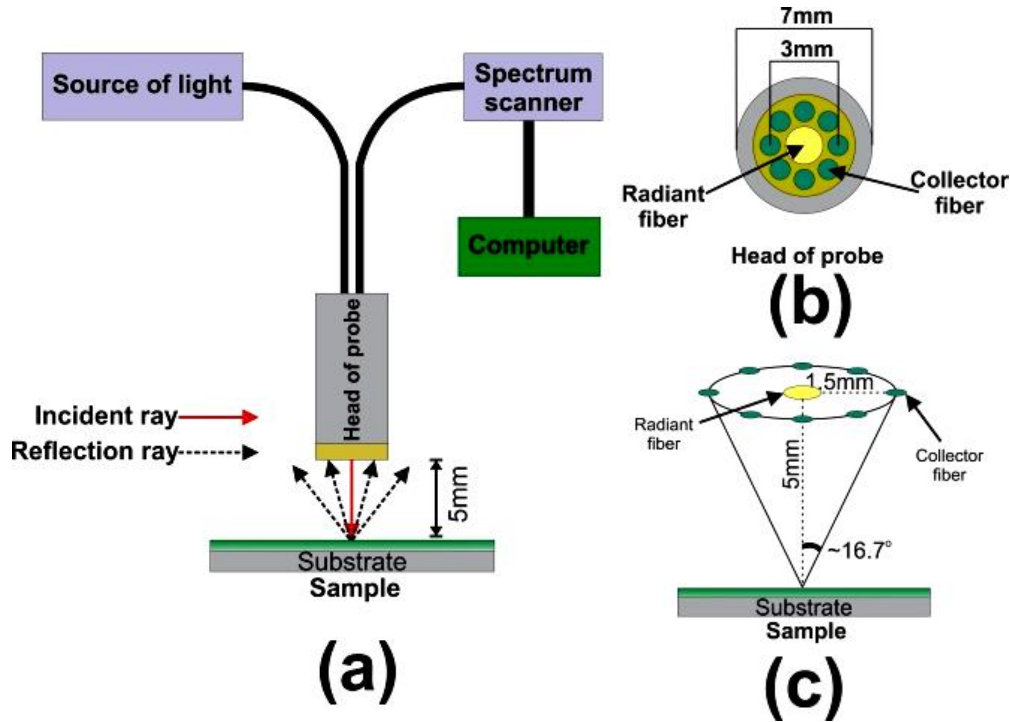


Fig. 3. The configuration of optical reflectometer. (a) The optical reflectometer working mechanism, (b) The probe head components, (c) fibers and sample at measurement configuration (color online)

The BST behaves like varistor in high voltages but at low voltages it still partially exhibits this behavior[49]. Therefore, electrical resistance measurements were performed in the voltage range of -10V to +10V. For this purpose, I-V characterization was conducted in dark and the following Ohm's law was used [50]:

$$R = \frac{V}{I} \quad (6)$$

where R is electrical resistance, I is electrical current, and V is applied voltage to resistor.

Reflection intensity and the peak wavelength of the reflection spectrum from blank and deposited substrates were measured using normal linear reflectometry[47], [48]. The samples reflection intensity ratio versus incident light intensity in peak wavelength has been calculated. The reflectometer configuration is shown in Fig. 3(a). Fig. 3(b) shows the locations of the radiation fiber and collector fibers, as well as Fig. 3(c) shows the places of the fibers and the sample in the surface reflectance measurement configuration.

3. Results and discussion

3.1. Morphological analysis

SEM imaging was performed to investigate the effect of the oblique angle deposition method and substrate material on the surface morphology of samples. The layers thicknesses were estimated using cross-sectional images shown in Fig. 4. Surface structure roughness could be seen in micrographs (d), (f) of Fig. 4. Deposited layers on different substrates show different thicknesses. These results imply that two parameters are effective on the thickness of the layers, namely, the density of deposited material and the amount of deposited material on substrates surface. As tabulated in Table 1, considering the layers thickness deposited on various substrates with 0° deposition angle and also surface porosity values suggests that the density of the layers is the most probable cause of the thickness variation.

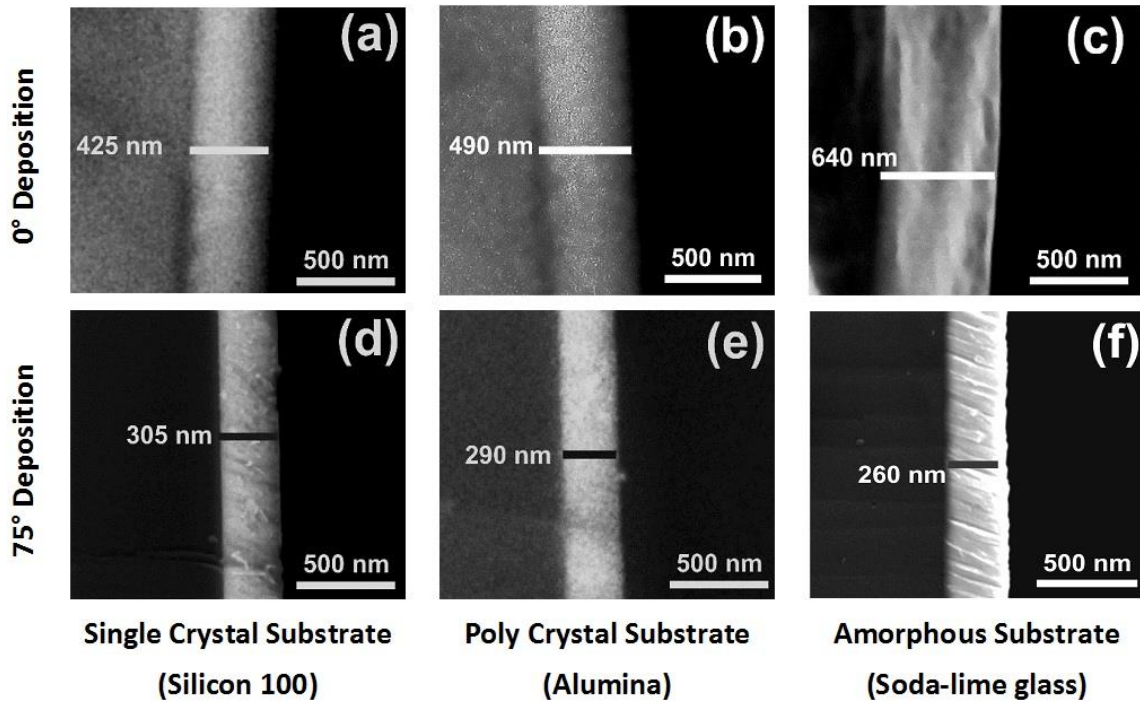


Fig. 4. Cross-sectional SEM micrographs of deposited BST thin films on (a) silicon wafer under 0° , (b) alumina wafer under 0° , (c) glass under 0° , (d) silicon wafer under 75° , (e) alumina wafer under 75° , and (f) glass under 75°

For the samples deposited with 0° , the amount of incident particle flux from the target to the substrate surface was constant and the difference in the thickness of this layer only is affected by the amount of deposited matter and the density of the formed layer. All the particle fluxes are not deposited on the substrate, and part of the flux may be dispersed in the deposition chamber in collision with the substrate. The density of the initially formed layers and the amount of surface porosity during deposition will affect the final density of the layers. According to Table 1, the surface porosity of the sample deposited on the amorphous substrate with 0° is higher than the other two samples deposited with 0° . This indicates that the density is lower in the underlying and interior layers formed, which increases the thickness in Fig. 4(c).

Fig. 4(e) shows no evidence of structure formation on films deposited on alumina substrate, which may be due to the high density of structures in the lower layers and the formation of large and continuous islands in those layers, the surface roughness is observable in corresponding planar image (Fig. 7(e)). In the cross-sectional SEM images shown in Figs. 4(a), 4(b) and 4(c) which are related to the samples deposited at 0° angle on silicon, alumina and soda lime glass substrates respectively, no special structure could be identified due to the absence of initial random seeds in the early stages of the layer deposition[36], [37], [51], [52].

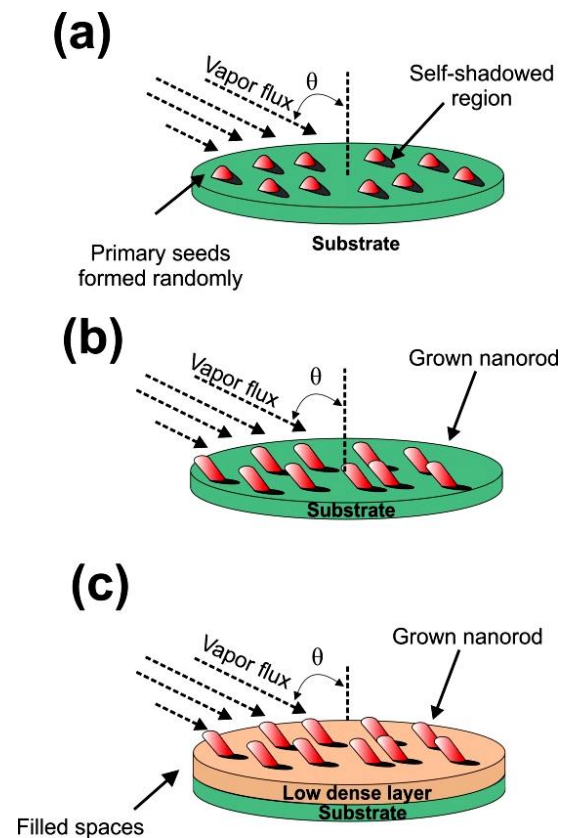
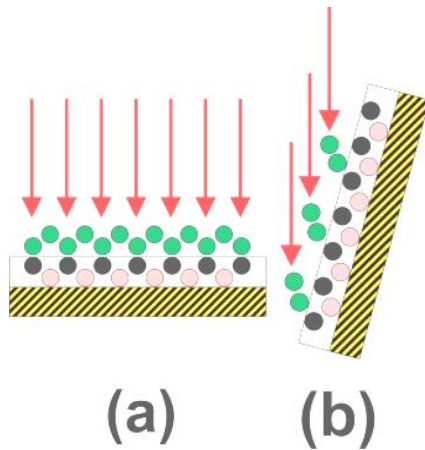


Fig. 5. Proposed nanorods formation in oblique angle deposition technique, (a) Random initial seeds formation[35], (b) Mass accumulation on seeds[35], (c) Dense nanostructures growth, mass accumulation on seeds and filling space between them with low density (color online)

Nanostructures formation in oblique angle configuration is illustrated in Fig. 5. Seeds deposition on the substrate at the initial stages of deposition process will result in shadowing effect for the upcoming material flux which consequently results in low density nanostructure formation (Fig. 5). Because the particles accumulate on the seeds, the nanostructures always grow faster than the free space therefore the surface of the low-density layers show higher roughness than high density layers deposited at 0° angles.



The main difference between the thickness of samples deposited with 0° and samples deposited with 75° is due to deposition angle and consequently the reduction of received material flux to the sample's surface (Fig. 6). Tilting the substrates results in the reduction of arrived particle flux per surface area of the substrate surface which consequently results in reduced layer thickness in comparison to layers deposited at regular deposition mode (Fig. 6). In the schematic difference of Figs. 6(a) and 6(b), we can see the influence of the substrate angle (the incidence angle of the material flux with the sample surface) on the structure formation and the preferred orientation of the crystal planes in Fig. 6 and GIXRD analysis results.

Fig. 6. Dependence of structure formation from particle flux on surface area as a function of the substrate angle, (a) Cross section view of deposition at normal incident angle, (b) Cross section view of deposition on tilted substrate (color online)

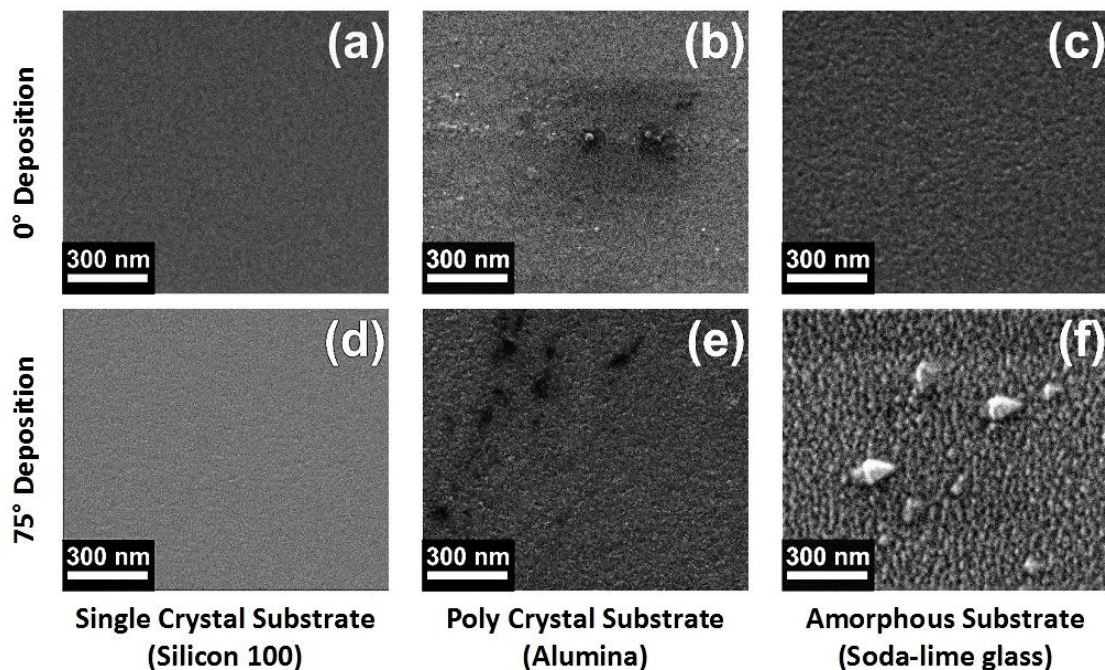


Fig. 7. Planar SEM micrographs of deposited BST thin films on (a) silicon wafer under 0° , (b) alumina wafer under 0° , (c) glass under 0° , (d) silicon wafer under 75° , (e) alumina wafer under 75° , and (f) glass under 75° [35]

Fig. 7 shows that the structures were formed on the surface of substrate. These structures have a flake-like shape and a direction opposite to the vapor flow direction and asymmetric shapes. In Fig. 7 (f) can be seen clearly

that these structures arranged uniformly on the surface. White big particles apparent in Fig. 7 (f) are related to pollution on the substrate surface before deposition and particles accumulation on these pollutions where larger

seeds cause larger structure growth. Surface roughness and structures observed in Figs. 7(d), 7(e), and 7(f) were predictable concerning the layer deposition configuration for the deposited samples at 75° angle. In the Fig. 7(c) sample the presence of surface roughness and structure can be due to kind and the crystalline state of substrate[16], as well as the nanorods formation rate on the substrate surface depends on the kind of deposited material. The use of a collimator causes the particles incident to be perpendicular on the substrate surface and first resulting masses formation as island form. In Figs. 7(a) and 7(b), the lack of roughness and structure can be due to the absence of random initial seeds in the early stages of layer deposition on the substrate surface[18], [36], [37], [51], [52].

Surface height profiles of samples in the 3-dimensional form are shown in Fig. 8. As can be seen

roughness, dispersion of masses, and variance of heights in the deposited layer for the samples coated with 0° is less than deposited layers coated with 75° . Roughness is a function of growth conditions, particles incident geometry, and substrate features (atoms configuration in substrate surface). In (d), (e), and (f) micrographs of Fig. 8 structures height exhibit uniform roughness on the surface of samples. Fig. 8(c) shows the matching of roughness with the result of Fig. 7(c). Figs. 8(a) and 8(b) also show the lowest amount of roughness, which corresponds to the samples deposited at 0° angle formed without any random initial seeds. Structures formation causes roughness at the surface of the layer, which is caused by differences in the rate of structures growth and the filling of space between structures by the matter (Fig. 5). The highest points are the brighter and the deepest points are darker in Fig. 8 micrographs.

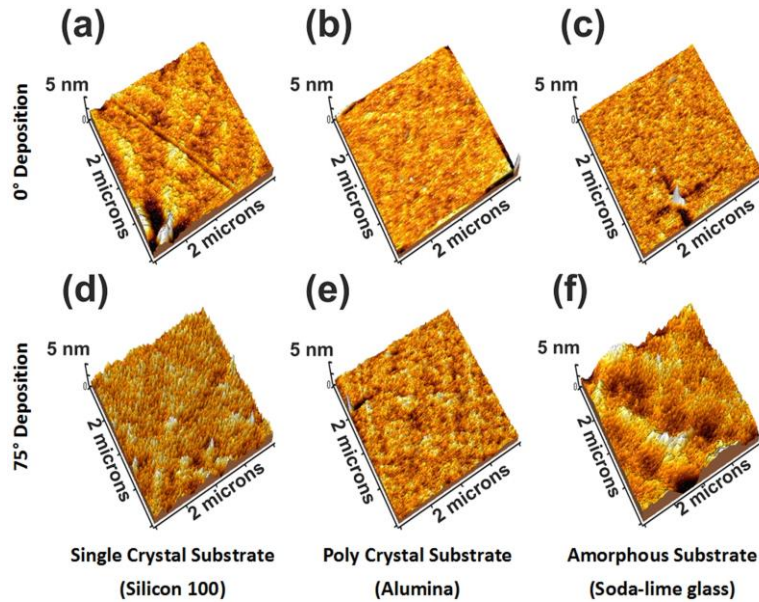


Fig. 8. 3D-AFM micrographs of deposited BST thin films on (a) silicon wafer under 0° , (b) alumina wafer under 0° , (c) glass under 0° , (d) silicon wafer under 75° , (e) alumina wafer under 75° , and (f) glass under 75° (color online)

Surface porosity percentage depends on peak to pit value and distance between surface structures and it can show empty volume on the surface[45], [46]. Calculated values for porosity are expressed in Table 1 by using equation 5. The volume of porosity in samples surface increased for tilted substrates during deposition and the

reason is stated in Fig. 5. Porosity increasing was predictable by the deposition process and condition of structure formation. By comparing roughness and surface porosity values in Table 1, a direct relation between roughness and surface porosity is found.

Table 1. Thickness, roughness and surface porosity obtained by AFM and SEM for deposited samples

sample	Deposition degree	Substrate crystalline type	Thickness (nm)	Roughness (nm)	Surface porosity (%)
a	0°	Single	425	0.122	11
b		Poly	490	0.684	17
c		Amorphous	640	1.012	28
d	75°	Single	305	4.521	62
e		Poly	290	3.143	35
f		Amorphous	260	3.978	54

3.2. Structural characterization

The formation of crystal structures of the deposited layers can be engineered by the type of substrates and parameters like crystal structure and lattice constant[22]. Based on the used patterns for matching, it is proved that the deposited films are polycrystalline-containing perovskite (BST) phases[27], [53], [54]. if the lattice constant and crystal network of the substance under sediment were close to the substrate[55]–[60], layers can grow similar to the structure of substrates in the deposition process under regular conditions[22]. Comparing patterns

of samples sputtered at the same angles can see that crystal planes of BST formed layers are different. In Fig. 9, the (BST 111) and (BST 200) planes are mostly oriented in patterns (a) and (b), and the (BST 110) plane is mostly oriented in pattern (c). Substrate angle change also can make different preferred orientations than deposition at 0° pose. In the new orientations, some peaks disappeared, appeared and some intensity of them changed. These new orientations are the result of structure formation on random seeds and collision angle than substrate planes (Fig. 6). Expressed crystallite size and strain in Table 2 were obtained by using Equation 1.

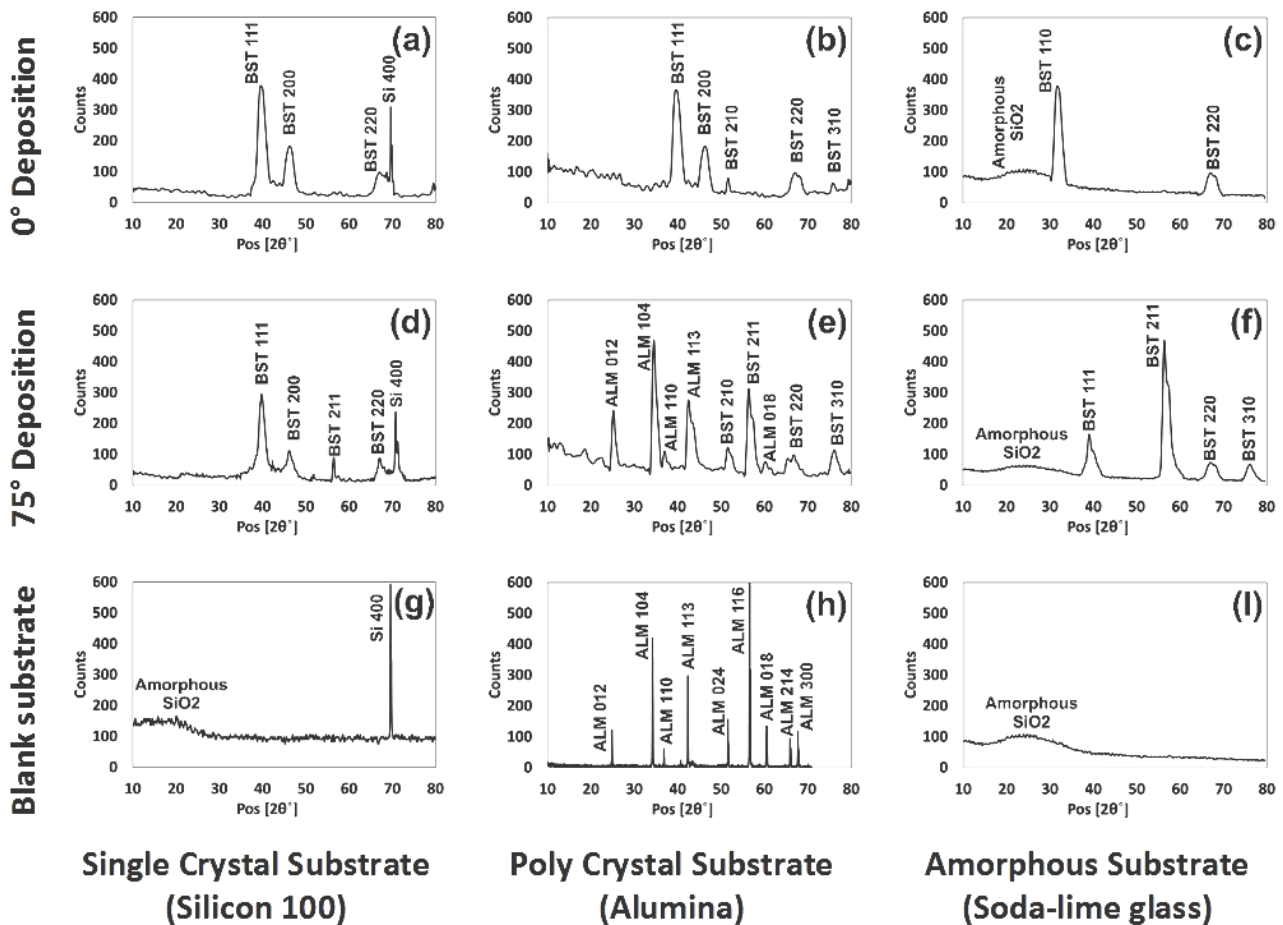


Fig. 9. GIXRD patterns (10° – 80°) of deposited BST thin films on (a) silicon wafer under 0° , (b) alumina wafer under 0° [35], (c) glass under 0° , (d) silicon wafer under 75° , (e) alumina wafer under 75° [35], (f) glass under 75° and patterns of blank substrate (g) silicon wafer, (h) alumina wafer, (i) soda-lime glass

The substrate effects can be observed in patterns (a), (c), (d), (e), and (f) of Fig. 9. The substrate-related peaks are visible in diffraction patterns due to the low thickness of the thin layers and the high density of the planes. In Fig. 9, for the pattern (a) and (d) because of the existence of one plane with high intensity that is related to the silicon substrate[61], [62], its peak (Si [400]) is seen in the pattern of deposited samples on silicon under 0° and 75° . In Fig. 9(g), the amorphous SiO₂ peak seen is because of the formation of a passive layer from silicon oxide on the

surface of the wafer under the atmosphere. In Fig. 9(e) take the angle by the substrate and reduce material flow received on the substrate surface resulting in a decrease of BST layer thickness, so the peaks of alumina substrate rise in the pattern. Crystallite size and strain do not have any trend in deposited layers and the positive value for the strain is an indication of tensile strain and the negative value is an indication of compressive strain[63], [64]. The low value of slope means that the internal strain is negligible[65].

Table 2. The Preferred plane, crystallite size and strain from GIXRD patterns for the deposited samples

sample	Deposition degree	Substrate crystalline type	Crystallite size (nm)	Strain (%)	Preferred plane
a	0°	Single	39	2.16	111
b		Poly	26	-1.49	111
c		Amorphous	46	2.27	110
d	75°	Single	82	1.02	111
e		Poly	42	0.11	211
f		Amorphous	56	1.41	211

3.3. Optical analysis

Fig. 10 shows the raw spectrum that radiated on the surface of the samples from the spectrometer for measuring the reflectance of theirs. The mechanism of the reflectometer device is shown in Fig. 3(a). The reflectometer guided this spectrum of light by an optical fiber on top of the surface at a vertical distance (5mm). The radiated incident beam on the surface of samples from the fiber is a mix of different wavelengths with the same intensity as Fig. 10.

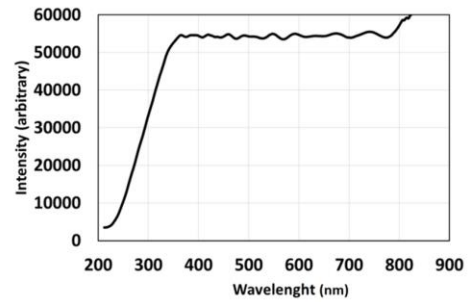


Fig. 10. Radiated raw spectrum on samples from spectrometer

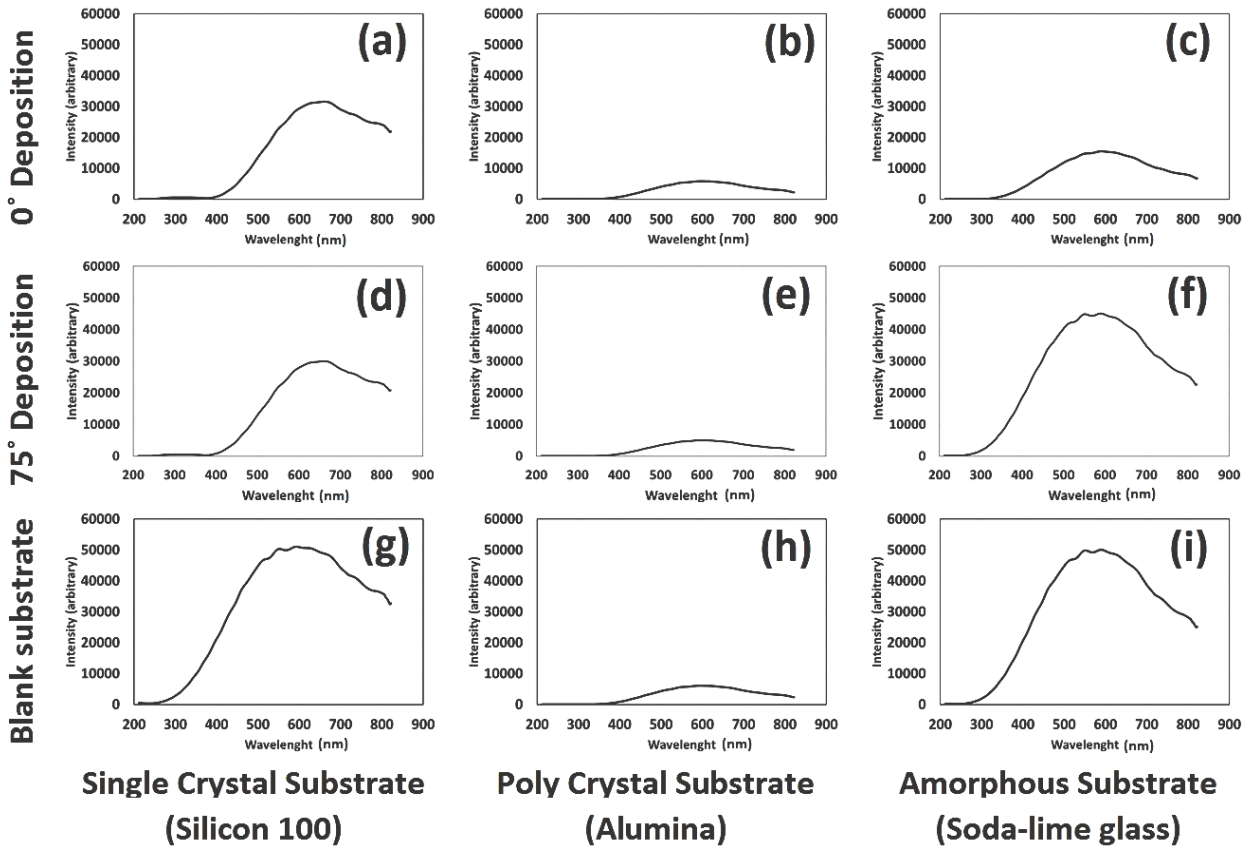


Fig. 11. Reflection spectrums of deposited BST thin films on (a) silicon wafer under 0°, (b) alumina wafer under 0°, (c) glass under 0°, (d) silicon wafer under 75°, (e) alumina wafer under 75°, (f) glass under 75° and reflection spectrums of blank substrate (g) silicon wafer, (h) alumina wafer, (i) soda-lime glass

Collector fibers placed around a flat circle on top of the surface and the location of the collector fibers relative

to the incident area of the beam with a 16.7° diffract angle from the incident beam are shown in Fig. 3(c). After

reflection from the surface, this spectrum is collected by other optical fibers which are placed around the radiant optical fiber called collector fibers (Fig. 3(b)). Collector fibers connect to a probe that scanned any wavelength in the specified range (200-825 nm). In Fig. 11, the 75° glass substrate sample (f) is more reflective than the 0° glass substrate sample (c) because the glass substrate is more polished and reflector than the BST layer and in sample (f) the substrate plays a more effective role in the reflectance by reducing the BST layer thickness. In Fig. 11, the reflection patterns of (d) and (e) have decreased compared to the (a) and (b) patterns, despite the decrease in the thickness of the BST layers due to the increased light absorption in the spaces between the BST nanostructures[66]–[68].

Determined reflection percentage and scattering peak by comparing the reflected spectrum with the radiated spectrum. The results of this comparison come in Table 3. According to Table 3 data, for all three substrates without coating, the maximum intensity of the reflectance spectrum is close to 594 nm values. After applying to coat on substrates at 0°, the maximum intensity wavelength did not change for coated sample on amorphous (glass) and polycrystalline (alumina) substrates but in coated sample on single crystal (silicon) substrate shifted to 673 nm. This shift occurs because the thickness is smaller than the radiated wavelength[48] and the silicon wafer surface is like a mirror, also the coated sample at 75° has a peak shifted to 662 nm. Peak shifts for these samples are affected by the thin thickness[48] and surface nanostructures[43], [69], [70]. If the thickness is thinner than the incident radiation wavelength, the Bragg-Snell equation 7 can predict this behavior of the reflectance

spectrum[48], [71]. According to equation 8, deposited layers can change the effective refraction index[48]. The equations of refraction and reflection are given below[48], [71].

$$m\lambda = 2d\sqrt{n_{eff}^2 - \sin^2\theta} \quad (7)$$

$$n_{eff} = \sum_{i=1}^M F_i n_i \quad (8)$$

$$m\lambda = 2d \times n_{eff} \quad (9)$$

where n_{eff} is the effective refractive index, F is the fraction of layer compounds, θ is incident radiation angle, m is the order of diffraction, and d is layer thickness.

According to equation 8, the material of deposited layers can change the effective refraction index, also equation 9 show thickness changing can shift reflectance peak to a longer or shorter wavelength. Nanostructures dimensions and shape be leading to scattering incident rays and scattered rays after refraction in layers exit from various angles[71], [72], some rays are reflected from BST layers surface scatter by surface roughness like what happens in reflections from the surface of a metallic sphere. Part of the wavelength shift of the reflection peak is due to the scattering related to the size of the surface nanostructures, also the reason for the occurring reflection peak around the red spectrum values in visible light[73].

Table 3. Electrical resistivity, light reflectance percentage and reflectance peak wavelength for the deposited samples

sample	Deposition degree	Substrate crystalline type	Electrical Resistivity ($\frac{M\Omega}{cm}$)(30°C) (5V)	Reflectance (%)	Reflectance peak wavelength (nm)
a	0°	Single	12.6	57.2	673
b		Poly	1356	10.6	594
c		Amorph	1241	91.3	594
d	75°	Single	15.6	54.3	662
e		Poly	1537	10.1	594
f		Amorph	1408	82.2	590
g	Blank substrate	Single	8×10^{-6}	93.2	593
h		Poly	$\approx 1 \times 10^8$	11.1	594
i		Amorph	$\approx 1 \times 10^8$	28.3	590

3.5. Electrical properties analysis

The behavior of electric current was characterized by voltage changes. This is done using a simple configuration

between a voltage source and a picoammeter which is shown in Fig. 12(a).

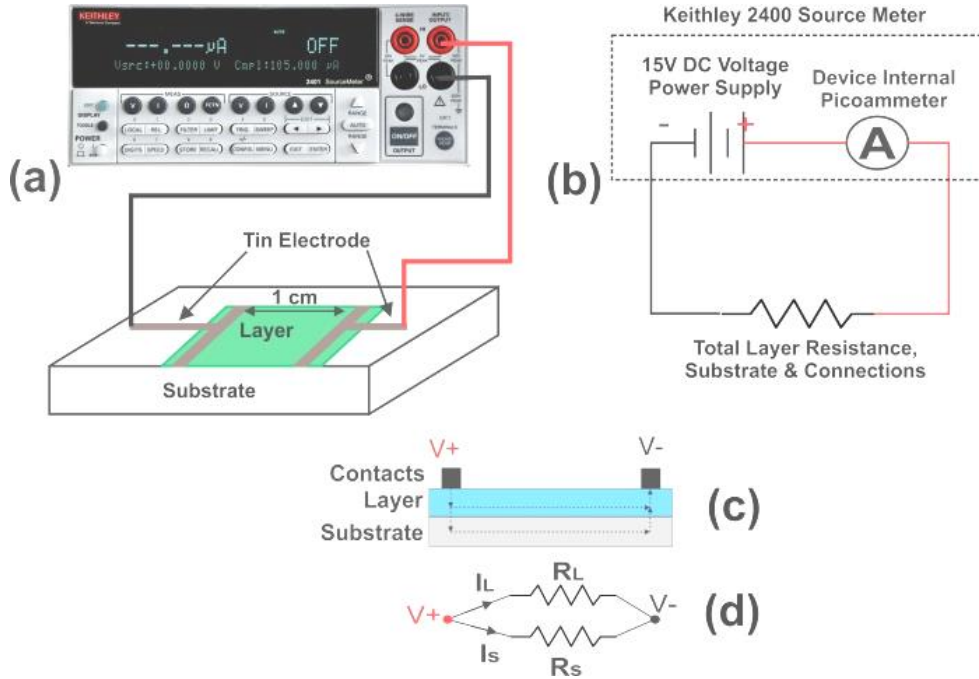


Fig. 12. (a) Schematic configuration of electrical resistivity measurement, (b) measurement circuit map, (c) Layers and connections schema, and (d) The equivalent circuit for electrical current passing through the layers (color online)

Electrical resistivity depends on the morphology[74], the electronic band structure of matter[75], the crystallite size (grain boundaries)[76], and the thickness of the layer[77]. Crystal structure plays a role in high symmetry paths of band structures with plane direction[78]. The number of grains has a direct relation with electrical resistivity, with grains increasing leading to increases in the length of the boundaries and consequently increasing the resistance; this concept is shown in Fig. 13. Increasing the thickness of the layer in this configuration for measuring electrical resistance gives more paths to

electron currents for passing at the layer, thus reducing the observed electrical resistance. Increasing layer thickness is a good parameter for reducing electrical resistance in this kind of measuring[77]. In deposited samples under 75° , formed low-density spaces between nanostructure causes increasing the electrical resistance of the layer because air instead of matter fills some spaces and air electrical resistivity is very higher than BST, trapped air between structures (oxygen vacancies) acts as a grain boundary and increases electrical resistance. The results of electrical resistivity measurements can be seen in Table 3.

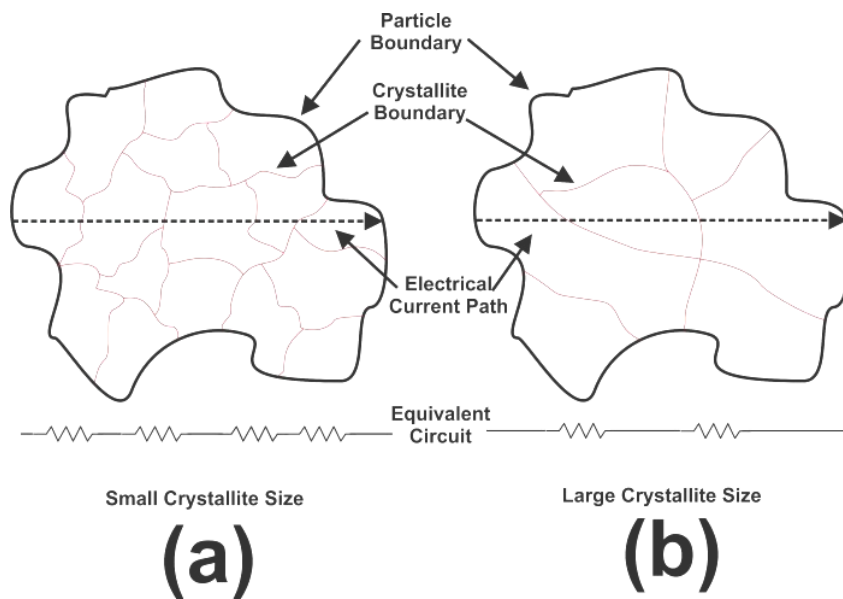


Fig. 13. The effect of crystallites size on electrical resistivity in 2D illustration of a single particle (a) Crystallites size is small and electrical current confront with more boundaries, (b) crystallites size is large and electrical current confront with fewer boundaries (color online)

After perusing obtained electrical resistivity expressed in Table 3, it was found that samples (a) and (d) deposited on silicon wafers have very low resistance in passing an electrical current. This low electrical resistance is due to the low substrate electrical resistance than the BST layer. Ohm's law in equation 6 stated that the current was inversely related to electrical resistance. You can see in Fig. 12(c) how the substrate helps to better pass current through the layer. For best concluding from the structural effect on electrical resistivity, the substrate electrical resistance must be either more than the BST layer or insulated. The substrate electrical resistance must be either more than the BST layers or insulated. In Fig. 12(d), the circuit equivalent to the substrate and layer resistances can be seen. If the R_S resistance value is higher than the R_L resistance value, which makes the R_S resistor act as an open circuit in the circuit and the major electrical current is passed by the R_L resistor and the passed electrical

current can largely represent the layer of electrical resistance. Assuming the R_L/R_S is very small and close to zero, the circuit electrical current equation can be rewritten as follows.

$$I = I_L + I_S = \frac{V}{R_L} + \frac{V}{R_S} = V \left(\frac{R_L + R_S}{R_L R_S} \right) \quad (10)$$

$$\frac{R_L}{R_S} \approx 0 \rightarrow I = \frac{V}{R_L} \quad (11)$$

where V has applied DC voltage, I is the total passed current of layer and substrate, I_L is the passed current through the layer, R_L is layer resistance, I_S is the passed current through the substrate, and R_S is substrate resistance.

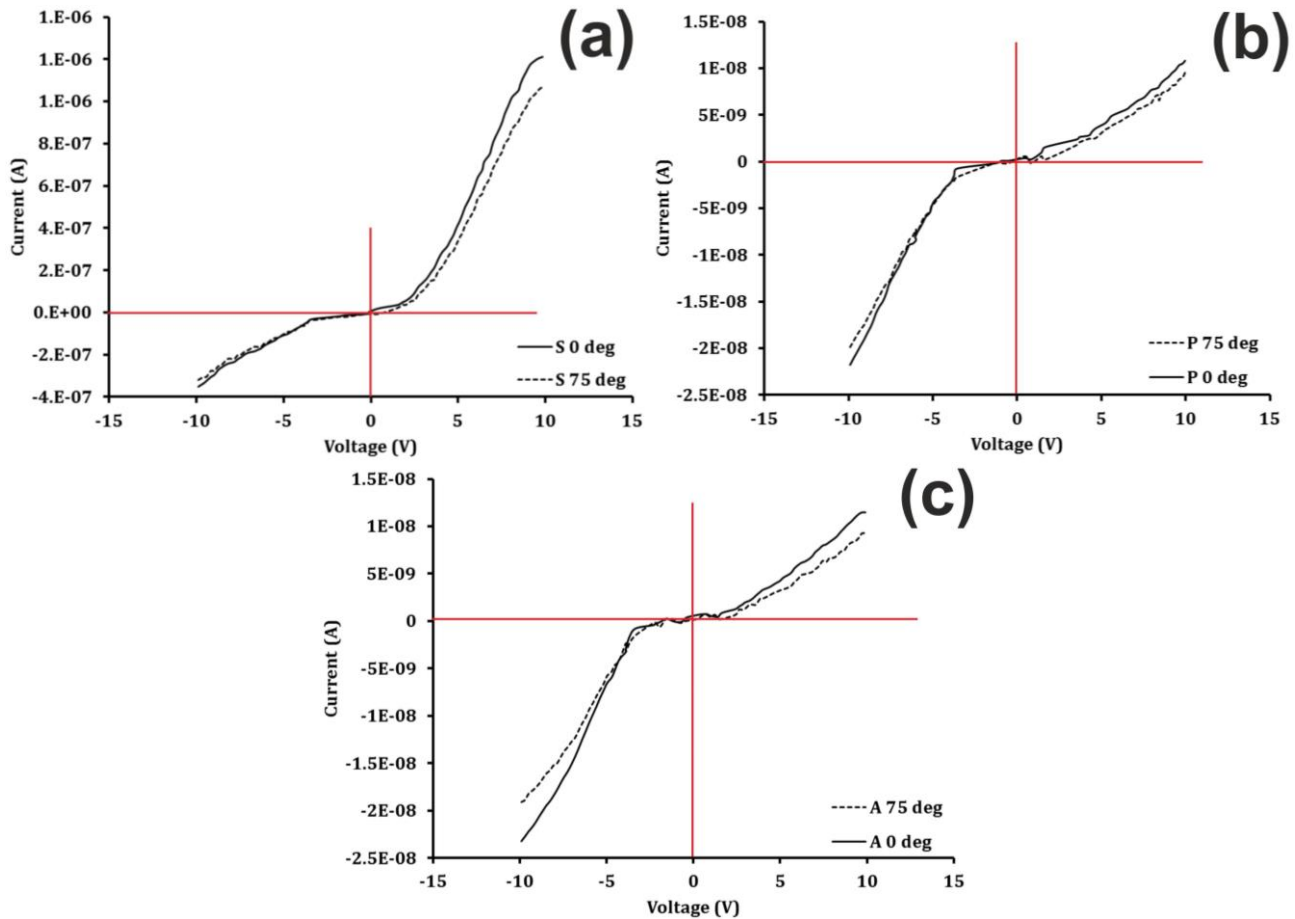


Fig. 14. I-V characteristic curves, dashed line is deposited in 75° and solid line is deposited 0° , (a) Single crystal substrate samples, (b) Polycrystalline substrate samples, and (c) Amorphous substrate samples (color online)

By comparing electrical resistivity between the samples (b), (c) and samples (e), (f) reported in Table 3 it can be observed that the layer on the polycrystalline substrate has less electrical resistivity than the layer on the amorphous substrate in both modes of regular deposition and oblique deposition. The observed phenomenon is not related to the electrical resistance of the substrate because

the polycrystalline substrates have higher electrical resistance than the amorphous substrates. This difference in electrical resistance can be justified by the concept of crystallite size which corresponds to expressed values in Table 2. In general, increasing the crystal size reduces the layer resistance in samples with similar conditions.

Fig. 14 shows the current-voltage (I-V) characterization diagrams. I-V curves show nonlinear behaviors that are similar to the behavior of diodes [79]. As can be seen in Figure 14(a), the deposited layer on the single crystal substrate has a slope of rapid changes in electrical current relative to the voltage at positive voltages and has a shorter branch at negative voltages, which behaves like a junction diode. Polycrystalline and amorphous substrate samples show the opposite behavior of single crystal substrate samples and the slope of electric current changes at steep negative voltages and has a shorter branch at positive voltages. The layer and substrate configuration shown in Fig. 12(c) acts like an n-p junction diode in the voltage in the range of +10V to -10V. The difference between the diagram curves of the samples with amorphous and polycrystalline substrates and the sample of single crystal substrate is due to the effect of silicon substrates on the passage of current through the BST layer, which turns it into the result of a junction between two semiconductor materials (a diode) [80], but in other samples, the electrical resistance of the substrate is so high that it is practically insulating and has no role in the current passing through the BST layer, and the observed curve belongs purely to the intrinsic electrical properties of the BST layer.

4. Conclusion

In summary, SEM micrographs show that thin film deposited on the polycrystalline substrate at 0° has a smaller grain size (26 nm) and higher electrical resistivity (1356 M Ω) than thin films deposited on the amorphous substrate at 0° which respectively is 46 nm and 1241 M Ω . While the thickness of the formed layer on the glass, polycrystalline alumina, and single crystal silicon substrate at 0° is 640 nm, 490 nm, and 425 nm respectively, the thickness of the formed layer at the oblique angle of 75° is 260 nm, 290 nm, and 305 nm respectively which is attributed to the change in the density of the formed layers due to the crystal planes orientation change by deposition angle. The thin films deposited on the single crystal substrate with 0° and 75° have the same crystal orientation, while deposited thin films on the amorphous substrate have different orientations in different deposition angles.

The roughness of the deposited thin films at 0° on the single crystalline silicon, polycrystalline alumina, and amorphous glass is 0.122 nm, 0.684 nm, and 1.012 nm respectively and for thin films deposited at 75° reached the values of 4.521 nm, 3.143 nm, and 3.978 nm. The ratio changing of the empty spaces in thin films and compounds affects effective refractive index change and causes displace the peaks of the reflection spectrum.

Acknowledgments

This research work has been supported by a Research Grant (No. G282839) from the Materials and Energy

Research Center (MERC), Karaj, Iran. Thanks to Ms. Nasim Samadi for editing the text of the current investigation.

References

- [1] P. S. Berdonosov, E. S. Kuznetsova, V. A. Dolgikh, A. V. Sobolev, I. A. Presniakov, A. V. Olenev, B. Rahaman, T. Saha-Dasgupta, K. V. Zakharov, E. A. Zvereva, O. S. Volkova, *Inorg. Chem.* **53**(11), 5830 (2014).
- [2] W. Nan, Y. Niu, H. Qin, F. Cui, Y. Yang, R. Lai, W. Lin, X. Peng, *J. Am. Chem. Soc.* **134**(48), 19685 (2012).
- [3] M. C. Plante, R. R. LaPierre, *Nanotechnology* **19**(49), 495603 (2008).
- [4] E. L. Belokoneva, *Cryst. Res. Technol. J. Exp. Ind. Crystallogr.* **43**(11), 1173 (2008).
- [5] H. L. Zhuang, M. D. Johannes, M. N. Blonsky, R. G. Hennig, *Appl. Phys. Lett.* **104**(2), 22116 (2014).
- [6] M. Gao, Y. Li, M. Guo, M. Zhang, X. Wang, *J. Mater. Sci. Technol.* **28**(7), 577 (2012).
- [7] D. Li, T.-S. Chung, R. Wang, *J. Memb. Sci.* **243**(1-2), 155 (2004).
- [8] D. Portehault, S. Cassaignon, E. Baudrin, J.-P. Jolivet, *J. Mater. Chem.* **19**(16), 2407 (2009).
- [9] G. Wu, J. Wang, J. Shen, T. Yang, Q. Zhang, B. Zhou, Z. Deng, B. Fan, D. Zhou, F. Zhang, *Mater. Res. Bull.* **36**(12), 2127 (2001).
- [10] Y.-C. Chan, H.-W. Chen, P.-S. Chao, J.-G. Duh, J.-W. Lee, *Vacuum* **87**, 195 (2013).
- [11] S. Yan, Y. J. Shang, X. F. Xu, X. Yi, X. Y. Le, *Nucl. Instruments Methods Phys. Res. Sect. B: Beam Interact. with Mater. Atoms* **272**, 450 (2012).
- [12] F.-S. Chien, C.-L. Wu, Y.-C. Chou, T. T. Chen, S. Gwo, W.-F. Hsieh, *Appl. Phys. Lett.* **75**(16), 2429 (1999).
- [13] A. Kawahara, Y. Takahashi, Y. Hirano, M. Hirano, T. Ishihara, *Solid State Ionics* **190**(1), 53 (2011).
- [14] H. Wiklund, T. Uesaka, *Nordic Pulp and Paper Resources Journal* **27**(2), 403 (2012).
- [15] M. Cargnello, V. V. Doan-Nguyen, T. R. Gordon, R. E. Diaz, E. A. Stach, R. J. Gorte, P. Fornasiero, C. B. Murray, *Science* **341**(6147), 771 (2013).
- [16] Y. Gao, S. He, P. Alluri, M. Engelhard, A. S. Lea, J. Finder, B. Melnick, R. L. Hance, *J. Appl. Phys.* **87**(1), 124 (2000).
- [17] Y. Kobayashi, Y. Iizuka, T. Tanase, M. Konno, *J. Sol-Gel Sci. Technol.* **33**(3), 315 (2005).
- [18] A. Barranco, A. Borrás, A. R. Gonzalez-Elipe, A. Palmero, *Prog. Mater. Sci.* **76**, 59 (2016).
- [19] L. Radhapiyari, A. R. James, O. P. Thakur, C. Prakash, *Mater. Sci. Eng. B* **117**(1), 5 (2005).
- [20] M. Enhessari, A. Parviz, K. Ozaee, A. H. Habibi, *Int. J. Nano. Dimens.* **2**(2), 85–103. (2011).
- [21] S. Li, Y. Yang, S. Wang, W. Liu, *J. Funct. Mater.* **38**(6), 921 (2007).
- [22] A. V. Tumarkin, A. A. Odinet, *Phys. Solid State*

- 60(1), 87 (2018).
- [23] Y. Zhang, M. Wang, X. Lin, W. Huang, *J. Mater. Sci. Technol.* **28**(1), 67 (2012),
- [24] Y. B. Zheng, S. J. Wang, L. B. Kong, S. Tripathy, A. C. H. Huan, C. K. Ong, *J. Electroceramics* **16**(4), 571 (2006).
- [25] L. Dai, S. Wang, P. Shu, Z. Zhong, G. Wang, G. Zhang, *Chinese Sci. Bull.* **56**(21), 2267 (2011).
- [26] T.-H. Fang, W.-J. Chang, C.-M. Lin, L.-W. Ji, Y.-S. Chang, Y.-J. Hsiao, *Mater. Sci. Eng. A* **426**(1–2), 157 (2006).
- [27] T. Zhang, H. Gu, J. Liu, *Microelectron. Eng.* **66**(1–4), 860 (2003),
- [28] Fangqi Gao, Jiadai An, in 2016 IEEE Advanced Information Management, Communicates, Electronic and Automation Control Conference (IMCEC), Oct. 2016, p. 1808.
- [29] I. Norezan, A. K. Yahya, M. K. Talari, *J. Mater. Sci. Technol.* **28**(12), 1137 (2012),
- [30] A. Kurniawan, D. Yosman, A. Arif, J. Juansah, *Procedia Environ. Sci.* **24**, 335 (2015).
- [31] T. Liu et al., *Mater. Sci. Eng. B* **176**(5), 387 (2011).
- [32] D. Roy, S. B. Krupanidhi, *Appl. Phys. Lett.* **62**(10), 1056 (1993).
- [33] H. J. Cho, J. B. Park, S. S. Yu, J. S. Roh, H. K. Yoon, ISAF 2000, Proceedings of the 2000 12th IEEE International Symposium on Applications of Ferroelectrics (IEEE Cat. No.00CH37076), **1**, p. 55.
- [34] K. Yao, R. Toole, P. Basnet, Y. Zhao, *Appl. Phys. Lett.* **104**(7), 073110 (2014).
- [35] M. Bordbari, M. J. Eshraghi, N. Naderi, A. Sedaghat Ahangari Hossein Zadeh, *Mater. Res. Express* **6**(2), 025009 (2019).
- [36] F. Maudet, B. Lacroix, A. J. Santos, F. Paumier, M. Parailous, S. Hurand, A. Corvisier, C. Marsal, B. Giroire, C. Dupeyrat, R. García, *Appl. Surf. Sci.* **520**, 146312 (2020).
- [37] M. Suzuki, *J. Nanophotonics* **7**(1), 73598 (2013).
- [38] C. Patzig, T. Karabacak, B. Fuhrmann, B. Rauschenbach, *J. Appl. Phys.* **104**(9), 094318 (2008).
- [39] C. Guozhong, *Nanostructures and nanomaterials: synthesis, properties and applications*, World scientific, 2004.
- [40] M. Eshraghi, M. R. Derakhshandeh, *J. Adv. Mater. Technol.* **6**(3), 79 (2017).
- [41] J. H. Won, S. H. Paek, Y. S. Hwang, K. K. Kim, Y. S. Cho, *J. Mater. Sci. Mater. Electron.* **6**(3), 161 (1995).
- [42] F. Challali et al., *Thin Solid Films* **518**(16), 4619 (2010).
- [43] P. Fallahazad, N. Naderi, M. J. Eshraghi, *J. Alloys Compd.* **834**, 155123 (2020).
- [44] Y. T. Prabhu, K. V. Rao, V. S. S. Kumar, B. S. Kumari, *World J. Nano Sci. Eng.* **4**(1), 21 (2014).
- [45] B. Bhushan, *Modern tribology handbook*, CRC Press, 2001.
- [46] M. Abdullah, K. Khairurrijal, *Indones. J. Phys.* **20**(2), 37 (2009).
- [47] J. Z. Xin, K. C. Hui, K. Wang, H. L. W. Chan, D. H. C. Ong, C. W. Leung, *Appl. Phys. A* **107**(1), 101 (2012).
- [48] Z. A. Sechrist, B. T. Schwartz, J. H. Lee, J. A. McCormick, R. Piestun, W. Park, S. M. George, *Chem. Mater.* **18**(15), 3562 (2006).
- [49] G. W. Dietz, M. Schumacher, R. Waser, S. K. Streiffer, C. Basceri, A. I. Kingon, *J. Appl. Phys.* **82**(5), 2359 (1997).
- [50] C. T. O'Sullivan, *Phys. Educ.* **15**(4), 237 (1980).
- [51] S. P. Stagon, H. Huang, *Nanotechnol. Rev.* **2**(3), 259 (2013).
- [52] M. Yilmaz, *Coatings* **9**(3), 198 (2019).
- [53] X.-R. Wang, Y. Zhang, T. Ma, C.-S. Deng, X.-M. Dai, *Ceram. Int.* **38**, S57 (2012).
- [54] A. Kaur, L. Singh, K. Asokan, *Ceram. Int.* **44**(4), 3751 (2018).
- [55] G. I. Tóth, G. Tegze, T. Pusztai, L. Gránásy, *Phys. Rev. Lett.* **108**(2), 25502 (2012).
- [56] J.-B. Lee, M.-H. Lee, C.-K. Park, J.-S. Park, *Thin Solid Films* **447**, 296 (2004).
- [57] D. Kan, I. Takeuchi, *J. Appl. Phys.* **108**(1), 14104 (2010).
- [58] J. Hornstra, W. J. Bartels, *J. Cryst. Growth* **44**(5), 513 (1978).
- [59] H. Miyoshi, Y. Horikoshi, *J. Cryst. Growth* **227**, 571 (2001).
- [60] Z. Fu, B. Lin, G. Liao, Z. Wu, *J. Cryst. Growth* **193**(3), 316 (1998).
- [61] B. Sahoo, W. A. Adeagbo, F. Stromberg, W. Keune, E. Schuster, R. Peters, P. Entel, S. Lüttjohann, A. Gondorf, W. Sturhahn, J. Zhao, *Phase Transitions* **79**(9-10), 839 (2006).
- [62] S. Mahmoudi, M. J. Eshraghi, B. Yarmand, N. Naderi, M. Askary-Paykani, *J. Alloys Compd.* **803**, 231 (2019),
- [63] A. Khorsand Zak, W. H. Abd. Majid, M. E. Abrishami, R. Yousefi, *Solid State Sci.* **13**(1), 251 (2011),
- [64] M. Taherkhani, N. Naderi, P. Fallahazad, M. J. Eshraghi, A. Kolahi, *J. Electron. Mater.* **48**(10), 6647 (2019).
- [65] J. I. Langford, R. J. Cernik, D. Louër, *J. Appl. Crystallogr.* **24**(5), 913 (1991).
- [66] R. Yu, Q. Lin, S.-F. Leung, Z. Fan, *Nano Energy* **1**(1), 57 (2012).
- [67] A. Peter Amalathas, M. M. Alkaisi, *Micromachines* **10**(9), 619 (2019).
- [68] G. Edman Jonsson, H. Fredriksson, R. Sellappan, D. Chakarov, *Int. J. Photoenergy*, **2011**, 1-11 (2011).
- [69] E. A. Martín-Tovar, E. Denis-Alcocer, E. Chan y Díaz, R. Castro-Rodríguez, A. Iribarren, *J. Phys. D: Appl. Phys.* **49**(29), 295302 (2016).
- [70] C. Charles, N. Martin, M. Devel, J. Ollitrault, A. Billard, *Thin Solid Films* **534**, 275 (2013).
- [71] G. Mayonado, S. M. Mian, V. Robbiano, F. Cacialli, *Am. Assoc. Phy. Teach. under a Creat. Commons Attr. 3.0 Licens.*, 2015.
- [72] P. L. Dawson, J. C. Acton, in *Proteins in Food Processing*, Elsevier, 2018, p. 599.

- [73] H.-J. Koo, J. Park, B. Yoo, K. Yoo, K. Kim, N.-G. Park, *Inorganica Chim. Acta* **361**(3), 677 (2008).
- [74] P. Kumar, A. Kumar, R. C. Meena, R. Tomar, F. Chand, K. Asokan, *J. Alloys Compd.* **672**, 543 (2016).
- [75] S. A. Holgate, *Understanding solid state physics*, CRC Press, 2009.
- [76] H. Zeng, Y. Wu, J. Zhang, C. Kuang, M. Yue, S. Zhou, *Prog. Nat. Sci. Mater. Int.* **23**(1), 18 (2013).
- [77] D. Chaverri, A. Saenz, and V. Castano, *Mater. Lett.* **12**(5), 344 (1991).
- [78] Y. Hinuma, G. Pizzi, Y. Kumagai, F. Oba, I. Tanaka, *Comput. Mater. Sci.* **128**, 140 (2017).
- [79] Gerold W. Neudeck, *The PN Junction Diode*, 2nd Edition., **II**, Addison-Wesley, 1989.
- [80] I. R. Putra, H. Syafutra, H. Alatas, *Procedia Environ. Sci.* **33**, 607 (2016).

*Corresponding author: eshr56@gmail.com